IEEE Access
Multidisciplinary ⋮ Rapid Review ⋮ Open Access Journal

Received May 5, 2021, accepted May 18, 2021, date of publication May 27, 2021, date of current version June 8, 2021.

Digital Object Identifier 10.1109/ACCESS.2021.3084528

Temporal Solar Photovoltaic Generation Capacity Reduction From Wildfire Smoke

DANIEL L. DONALDSON[1], (Graduate Student Member, IEEE), DAVID M. PIPER[2], AND DILAN JAYAWEERA[1], (Senior Member, IEEE)

[1]Department of Electronic, Electrical and Systems Engineering, University of Birmingham, Birmingham B15 2TT, U.K.
[2]Southern California Edison, Rosemead, CA 91770, USA

Corresponding author: Daniel L. Donaldson (dld818@bham.ac.uk)

This work was supported by the University of Birmingham.

ABSTRACT Wildfire smoke and other particulate matter can substantially inhibit solar photovoltaic (PV) generation production. While solar PV facilities may not be located in areas with a high fire risk, smoke from wildfires can travel hundreds of kilometers impacting a large number of facilities. This paper proposes a geospatial wildfire PV capacity model to quantify the anticipated temporal reduction in PV capacity due to wildfire smoke. A case study using data for two time periods from the 2020 California wildfires and real utility scale solar generation data evidences the model's high accuracy. Results argue that wildfire smoke can cause significant temporal solar generation capacity reductions over wide geographic regions. Application of the proposed model to inform power system resiliency planning is demonstrated for two use cases: generation scheduling and siting. With meteorological service providers beginning to release smoke forecasts, our geospatial wildfire PV capacity model enables balancing authorities to make use of this information to proactively schedule generation to compensate for reductions in PV capacity. The trained model also produces geospatial derate maps that can enable generation developers to consider historical capacity derates due to smoke when making siting or planning decisions.

INDEX TERMS Photovoltaic power generation, power system operation, resilience, solar photovoltaic generation, wildfire smoke effects.

I. INTRODUCTION

Extreme wildfires are becoming an increasing risk to the safe and reliable operation of electric power systems worldwide. In the last few years some of the most extreme fire seasons on record have been seen in Australia, Brazil, Russia, and the Western United States [1]. While some transmission planning standards such as NERC TPL 001-5 in the US [2] consider extreme wildfires to be a high impact low probability (HILP) event, the need to proactively plan for the effect of extreme wildfires on modern power systems is growing.

The relationship between climate, anthropogenic effects, and wildfires remains complex. Some reports [1], [3] show a decline overall in the number of acres burned each year globally, but note that the trend varies significantly by region. Authors in [4] provide analysis highlighting differences across regions and identified anthropogenic increases in extreme Fire Weather Index days for 22% of burnable land area globally as of 2019 and project this to grow to 33-62% by the middle of the 21st century. In addition, authors in [5] found fire weather season length increased by 18.7% from 1979 to 2013. Such work suggests a heightened need for wildfire planning.

In 2020, the Western United States, experienced one of the worst wildfire seasons on record, with the state of California experiencing five of the six largest wildfires in its recorded history [6]. The largest of these fires spanned over 1 Million acres (4000 km^2) [6] and the smoke from these fires reached the East Coast of the United States before entering the jet stream and travelling across the Atlantic Ocean. This can be seen in Fig. 1 depicting smoke layers from the United States National Oceanic and Atmospheric Administration's (NOAA's) Hazard Mapping System (HMS) on September 14th, 2020 [7], [8].

At the same time, 2019 represented record levels of solar integration across the globe with stable growth in 2020 despite the Covid-19 pandemic [9]. With balancing authorities reliant on increasing levels of solar generation to

The associate editor coordinating the review of this manuscript and approving it for publication was Mahdi Pourakbari Kasmaei.

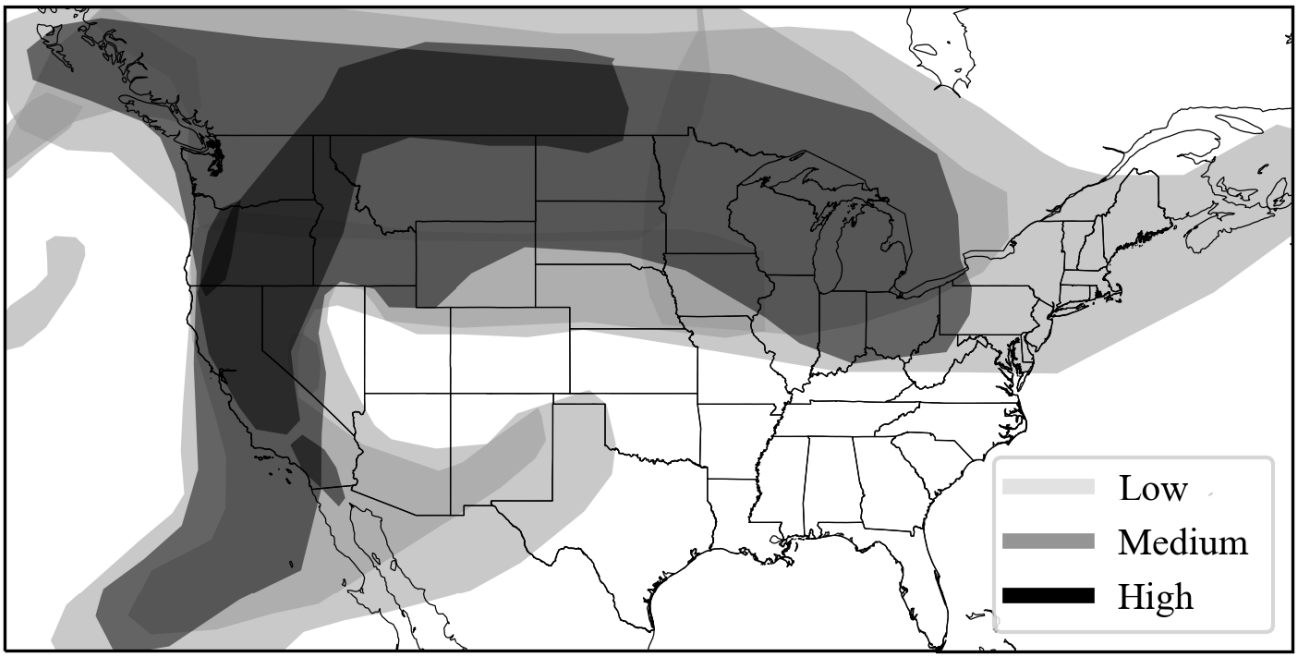

FIGURE 1. Smoke from wildfires spans the continental united states on September 14th 2020. Animated version showing entire summer period is available in the graphical abstract. Smoke layers from the NOAA HMS [7], [8].

serve electricity demand, wildfires present a new widespread risk to power system security due to the derate to solar production. This can cause inaccuracies in estimates of solar PV availability, placing additional strain on a system which may already be in a state of emergency due to infrastructure damage. In this paper we investigate the relationship between effective solar photovoltaic (PV) capacity and wildfire smoke using aerosol optical density (AOD) to quantify the amount of smoke present at a specific point in time.

By its very nature, the production of solar PV generation is directly dependent on meteorological factors such as irradiance, ambient temperature, wind speed, relative humidity and air mass along with their interaction effects. Authors in [10] show how incorporating each of these weather variables can enhance PV forecasts, but state that insolation and temperature are the most significant factors affecting solar PV generation. Extensive research has been carried out to determine the impact that each of these variables have on the overall performance. A review of studies evaluating the temperature dependency of PV generation is provided in [11]. Further assessment of the effects of humidity and wind speed was conducted in [12] noting that humidity can reduce efficiency by inhibiting the reception of the direct component of solar radiation and whereas wind speed can improve efficiency due to decreased cell temperature.

The significance of these factors varies based on the climate of the region where the PV generation is installed. For example, for windy regions, authors in [13] evaluated the impact of wind speed on PV capacity calculations for a windy city in Denmark and found that accounting for wind speed resulted in a 3.5% increase in PV capacity. For a region in the Northern United States, snow is a significant consideration and authors in [14] found annual losses ranging from 5-34% depending on the tilt angle and configuration of the installation. Standardized reference systems have been developed to provide a common framework for manufacturers to test the rated power output [15]. Therefore, when assessing PV capacity, efforts should be made to control for the climate variables present in the location of interest when possible to better identify the effects of an individual variable such as wildfire smoke.

Reductions in solar PV capacity can be caused by a variety of additional environmental variables including wildfires, however, previous research has largely been focused on clouds, dust and other forms of air pollution. Initial work on PV clouding effects demonstrated the large and rapid changes in generation from clouds [16]. More recently, authors in [17] detail various methods for forecasting solar production and the challenges induced from clouds. Researchers have continued to expand upon methods to integrate clouding effects into PV forecasts using more advanced deep learning methods to utilize sky imagery [18]. However, wildfires represent a different type of impact as they can be both natural disasters and anthropogenic (caused by humans) with [19] providing information on the cause of wildland fires in the United States. Furthermore, unlike clouds, the wildfires themselves pose a threat to the power system which can result in increased system stress. Hence it is important to consider the increased stress that wildfire smoke can cause as a result of reduced generation capacity during such extreme events.

Dust and air pollution can also greatly affect the performance of solar PV facilities. This can be observed as winds

carry dust from duststorms in the African Sahara to Europe causing temporal PV capacity degradation as described by authors in [20] and [21]. In [20], authors describe that such events can occur 5 to 15 times per year for several days and contributed to forecasting error of up to 5.3 GW when failing to consider dust. The amount of derate due to dust is assessed to be between 13 and 40% in [21] with higher reported values for facilities with parabolic trough configurations. However, geographically, most of these effects are limited to regions surrounding large deserts such the Sahara, Middle and Eastern Asia [22]. Similar to dust, researchers have studied the effects of air pollution often referred to as haze, identifying 20% capacity reductions in Eastern China [23]. An extensive field study using empirical data from Delhi and Singapore was conducted in [24] and extended to 16 cities around the world. This study found estimated reductions in insolation ranging from 2-9%. While both dust and air pollution do affect solar PV production, the impacts can be further compounded by the presence of wildfire smoke.

The temporal effects of wildfire smoke on solar PV capacity has received limited attention in previous research. Authors in [25] used a controlled burn in Australia to take sensor measurements on the impact on solar PV production for a single site showing a 27% reduction in output for a 1.56 kW solar PV facility. However, this study was localized in nature focusing on a single facility and fire. What remains to be seen, is the relationship between the magnitude and duration of wildfire induced smoke and the corresponding derate to solar production.

In initial efforts to answer this question, the United States Energy Information Administration (EIA) released a news release [26] highlighting correlation between PM2.5 emissions and wildfires and indicating 30% reductions in solar performance. However, the magnitude of the derate in the EIA study was derived from a comparison between statewide solar generation output between September and July 2020 which could be impacted by a variety of other factors such as curtailment and scheduled outages in addition to wildfire smoke. Furthermore, although the contribution of wildfires to overall PM2.5 emissions is increasing, other factors also contribute to PM2.5 [27].

In this work, we provide a framework which identifies the relationship between wildfire smoke and PV performance. Our paper provides the following contributions:

- proposal of a geospatial wildfire PV capacity model reflecting anticipated temporal derates to solar PV capacity due to wildfire smoke.
- an innovative framework enabling grid operators and balancing authorities to use this model during a wildfire to influence scheduling decisions and reserve requirements in the form of a geospatial smoke-derate map.
- propose a simplified geospatial nomogram for use in pre-planning and interconnection feasibility studies by developers to assess output reductions

The remainder of the paper is structured as follows: Section II details the methodology; Section III describes the case study which tests the efficacy of the model using actual data from recent California wildfires and real utility scale generating facilities; Section IV discusses the implications and benefits of this model and means to overcome some of the model limitations; Finally, Section V presents the conclusions, detailing the significant benefits of the proposed model.

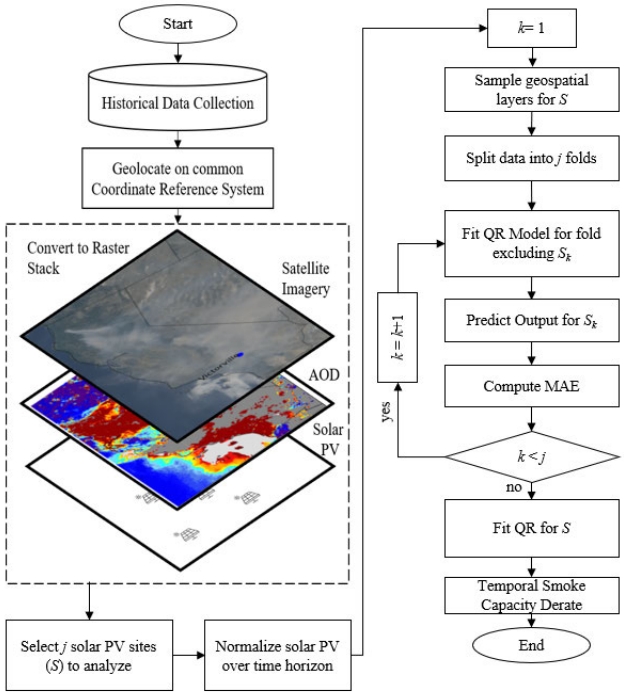

FIGURE 2. Brief overview of methodology for geospatial wildfire PV capacity model. Satellite imagery from NOAA GOES-17 satellite [28].

II. METHODOLOGY

This section aims to analyze the aerosol optical density at solar PV generating facilities during wildfire periods, and then study the corresponding solar PV power output characteristics. A visual depiction of the steps in the methodology can be found in Fig. 2

A. PRESENCE OF AEROSOLS DURING WILDFIRES

NOAA defines aerosol optical density as "a measure of the extinction of the solar beam by dust and haze. In other words, particles in the atmosphere (dust, smoke, pollution) can block sunlight by absorbing or by scattering light. Aerosol optical density tells us how much direct sunlight is prevented from reaching the ground by these aerosol particles" [29]. Aerosol optical density can vary on a scale from −1 to 5 [28] with 0.4 reflecting a hazy day and the average aerosol optical density over the continental US being 0.1-0.15 [29].

Satellite imagery is emerging as a valuable source for geospatial data as the resolution and quality of data continues to improve. In order to use satellite measurements at a specific location, the measurements must be converted into the appropriate orthographic plane. These calculations are relative to the data format produced by the satellite,

but detailed methodology describing the format of satellite imagery can be found in [28].

B. SOLAR PV POWER CAPACITY

Solar PV power capability is generally defined as a function of the physical specifications of a particular generating facility and the maximum expected solar irradiance on a particular day. This value varies seasonally and diurnally as a function of the suns position with respect to the earth. The Global Horizontal Irradiance (GHI) reflects the overall irradiance and is a function of Direct Normal Irradiance (DNI), Diffuse Horizontal Irradiance (DHI) and the solar zenith angle α. GHI can be calculated as [30]:

$$\text{GHI} = \text{DNI} \cdot cos(\theta_\alpha) + \text{DHI} \tag{1}$$

Furthermore, the Solar PV Power capacity can be impacted by other meteorological variables as described in [10]. The combination of physical parameters and meteorological variables results in a variation in maximum generating capability for each solar PV generating plant over a time period.

In order to compare performance of solar PV generating plants of different capacities across different time periods, a three-stage normalization process is proposed.

1) SEASONAL NORMALIZATION

In addition to the capacity of a PV facility changing from one plant to another, the effective capacity changes seasonally throughout the year due to the relative position of the sun. This means that the maximum expected output will vary as a function of the day of the year. To make an equivalent comparison of effective capacity over an extended time period, the capacity values should also be seasonally normalized.

One source of data to use to perform seasonal normalization is historical operating data for each facility for a period of several years. However, clean historical data may not be available for a sufficient period of time to develop a robust seasonal approximation. As maximum solar PV production is highly correlated with the clearsky GHI, an empirical distribution of the clear sky GHI can be used to calculate a further seasonal adjustment factor to use for normalization. The factor is calculated as in (2).

$$s_i = \frac{C_{max}}{C_i} \tag{2}$$

where s_i is the seasonal adjustment factor at time i; C_i is the clearsky GHI at the location closest to the plant for a specific hour during the study period; and C_{max} is the maximum clearsky GHI at that hour for that location across the study period. The clearsky GHI series from which C_{max} and C_i are sampled is produced by taking the average value for that location across the historical years available.

2) WEATHER NORMALIZATION

The capacity of PV generation facilities is affected by other meteorological variables in addition to irradiance [31]. In order to minimize the effect of these other variables on the capacity fluctuations and focus on the effects resulting from wildfire smoke, it is critical to normalize for these variables as well. Two meteorological variables (temperature and windspeed) are considered in the normalization process through the calculation of the PV cell temperature. When the cell temperature exceeds 25 °C, the efficiency of the generation is reduced by a factor of 0.5% per °C [11], [32]. In order to calculate the cell temperature and account for variation in ambient temperature, irradiance and windspeed the Sandia module temperature equations [33] are used as follows:

$$T_m = E[e^{\gamma_1 + \gamma_2 v}] + T_a \tag{3}$$

where T_m is the back-surface module temperature (°C); E is the plane-of-array (POA) irradiance (W/m2); γ_1 and γ_2 are empirically derived constants; T_a is the ambient temperature (°C); and v is the wind speed (m/s). Once the module temperature is calculated, a further correction must be applied to obtain the cell temperature as in:

$$T_c = T_m + \frac{E}{E_o}\Delta T \tag{4}$$

where T_c is the cell temperature inside the module (°C); E_o is the reference solar irradiance (1000 W/m^2); and ΔT is the temperature difference between the cell and the module back surface at an irradiance level of 1000 W/m^2.

3) MIN-MAX NORMALIZATION

The last stage of the normalization process relies on Min-Max normalization to transform the PV power output to allow equivalency in comparison across different plants. Min-Max normalization [34] converts $x = x_1, x_2, \ldots, x_n$ to a range of [0,1] via the formula in (5).

$$x_i' = \frac{x_i - x_{min}}{x_{max} - x_{min}} \tag{5}$$

where x_i' and x_i are the normalized and actual recorded solar power output at time i; x_{min} and x_{max} are the minimum and maximum power output within the fire study period n. This technique is highly interpretable as it maintains the original load shape.

C. WILDFIRE SMOKE PV RELATIONSHIP MODEL

This work proposes a model to characterize the relationship between aerosol optical density and solar PV generation output using quantile regression. This is the first key contribution. This model was selected due to the ability to minimize the effect of outliers and retain high accuracy in projecting the maximum PV output at high aerosol optical density. Other more complex deep learning and machine learning based models were considered but not ultimately selected as such models may be prone to overfitting due the size of the data used in this case study. Such models may be beneficial in the future for specific operating areas with larger amounts of historical data. The framework presented in this work is such that as further models are developed, they can be

readily integrated into the methodology as shown in Fig. 2. Our proposed model is compared to linear regression and piecewise linear regression benchmark models to evaluate its relative accuracy.

Quantile regression (QR) was proposed in [35] and facilitates a modeling of the full conditional distribution. QR has been used to forecast electricity demand [36] and solar irradiance [37]. The median quantile can be selected to compare with other deterministic models. QR for the τth quantile can be reflected as:

$$P_W(\tau) = \beta_0(\tau) + \sum_{v=0}^{p} \beta_v(\tau) x_v + \varepsilon \tag{6}$$

where τ is the quantile level; p represents the number of input variables; and $P_W(\tau)$ reflects the value of P_T below which the proportion of the conditional response population is τ. The parameters are estimated by minimizing the loss function for a particular quantile τ as in:

$$\hat{\beta}_\tau = \underset{\beta \in \mathbb{R}}{\operatorname{argmin}} \sum_{i=1}^{n} \rho_\tau (P_{W_i} - x_i^T \beta_\tau) \tag{7}$$

where ρ_τ is the pinball loss function for a quantile τ, where $\rho_\tau(z) = \tau z$ if $z \geq 0$ and $\rho_\tau(z) = (\tau - 1)z$ if $z < 0$.

Piecewise Linear Regression (PLR) uses several discrete linear segments to describe a one-dimensional (1D) dependent variable. In this case PLR allows for the slope of the relationship to change at higher densities of wildfire smoke. The PLR is formulated such that the function is continuous over the domain [38] and is as follows:

$$P_W(x) = \begin{cases} \beta_1 + \beta_2(x - b_1) & b_1 \leq x \leq b_2 \\ \beta_1 + \beta_2(x - b_1) + \beta_3(x - b_2) & b_2 < x \leq b_3 \\ \vdots & \vdots \\ \begin{bmatrix} \beta_1 + \beta_2(x - b_1) + \beta_3(x - b_2) \\ + \cdots + \beta_{c_b}(x - b_{c_b - 1}) \end{bmatrix} & b_{c-1} < x \leq b_{c_b} \end{cases} \tag{8}$$

where P_W is the anticipated power output of the PV generating plant in per unit accounting for wildfire smoke; c_b is the number of knots in the spline; x is the aerosol optical density; $b_0, b_1, \ldots, b_{c_b}$ are the location of the knots; and β are the slope coefficients. The set of equations is then solved for the unknown β that reduces the sum-of-square of the residuals.

A Linear Regression Model [39] was also developed to provide a basic benchmark to allow operators to compare the performance. The suitability of each model is tested using cross-validation. As the intensity of wildfire smoke is not evenly distributed across a given fire season, but dependent on the number of active fires at any given point in time, this relationship constitutes an unbalanced problem. Hence, the suitability of each of the proposed models is tested using stratified k-fold cross validation. Stratified k-fold cross validation seeks to ensure that the proportion of days with active wildfires within each fold is similar to the proportion found in the original distribution. Within each fold, mean absolute error (MAE) is computed as the error metric for the deterministic forecast.

III. THE IMPACT OF WILDFIRE SMOKE ON SOLAR PV CAPACITY

The efficacy of the methodology presented in Section II is demonstrated using real solar PV generation data during the 2020 wildfire season in California over two event periods: Scenario A) a two-week period in September covering the most significant fires; and Scenario B) an extended period covering the period from August 1st to September 28th. Analysis is conducted in python; data analysis is performed using the numpy [40] and pandas [41] packages; geospatial analysis was conducted using geopandas [42] and cartopy [43]; and visualization using matplotlib [44]. The models were specified and fit using statsmodels [45] for linear and quantile regression and pwlf [38] for the PLR. For PLR, the number of line segments was specified to be two, allowing the model to capture an initial rate of change at lower aerosol optical density and another rate as the aerosol optical density increases. The pwlf library uses the underlying scipy [46] library to calculate the optimal location of the knots via differential evolution.

A. CASE STUDY

1) WILDFIRES

The 2020 wildfire season in California contained many large wildfires with widespread impact concentrated in the months of August and September. For Scenario A, to match the geospatial location of the PV facilities which are predominantly located in Southern California a two-week period from September 1st to September 14th was selected. This period covers the start of three major fires: Creek Fire [48] - Largest single non-complex fire on record [6]; Bobcat Fire [50]; and the El Dorado Fire [49] with perimeters obtained from [47]. To enhance the robustness of the models developed, evaluate the sensitivity of such models to additional training data, and demonstrate the importance of the normalization process, based on the historical operating data available, a longer period from August 1st to September 28th (Scenario B) was also evaluated. Fig. 3 depicts the location of the 2020 wildfires in California in relationship to the PV sites selected.

2) SOLAR PV GENERATION

Data for solar PV in the state of California is retrieved from SCADA for ten PV generation facilities across four geographic areas. The names of urban regions near each of the PV facilities are used as labels rather than the specific location to maintain confidentiality of the individual facilities performance data. Data for each of the PV facilities is collected for the two week and two month case study periods. The three-stage normalization process described in Section II is performed for each of the ten PV facilities. As the sites are

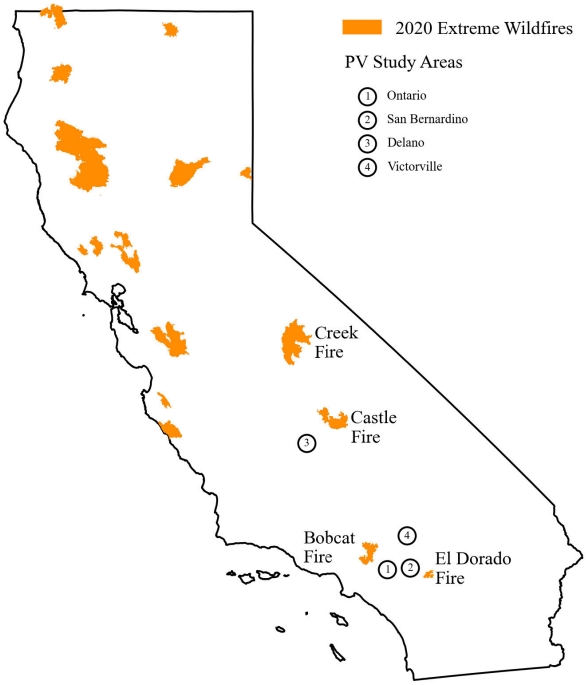

FIGURE 3. California's 2020 wildfire season is the worst in recorded history. Data for fire perimeters is from national interagency fire center (https://data-nifc.opendata.arcgis.com/) [47].

located in California weather can be especially hot during the summer months, with ambient temperature exceeding 45 °C. Weather used for the normalization process comes from the NASA's MERRA-2 renalysis [51]. As individual site specific information is not available, values of -3.47, $-.0594$ and 3 from [33] are used for γ_1,γ_2 and ΔT respectively. Historical clearsky GHI data for the period of 2005-2019 obtained from the National Solar Radiation Database is used to calculate the mean anticipated clearsky GHI for each PV site [52]. For Scenario A, seasonal normalization is performed, but expected to have more limited impact due to the shortened period. However, adjustments resulting from this process are expected to be more significant for Scenario B as the time period is much longer.

3) SATELLITE IMAGERY

For this work, satellite data is retrieved from NOAA's geostationary Earth-observing systems (GOES-17) satellite which became operational in 2019 [8]. GOES-17 covers the the full disk with 10 minute refresh rate. A faster refresh rate of 5 minutes for a 3000 km by 5000 km area covering the continental United States (CONUS) is also provided and used in this case study [28].

Two products are used for this work. The first is the aerosol optical depth. GOES-17 produces aerosol optical density data at 2 km grid resolution. The exact data retrieved is an image with pixel values identifying a measure of the extinction due to atmospheric aerosols at a wavelength of 550 nm for each specific point in time. This is represented as $\mathrm{AOD}_{lon,lat,i}$ where *lon* is the longitude and *lat* is the latitude. The second is the Cloud and Moisture Imagery Product. This is used to produce Red-Green-Blue (RGB) images of a particular time to allow visual inspection of the model results.

GOES aerosol optical density data is only produced when there is an absence of snow or clouds, for specific solar zenith angles and levels of surface reflectance. Specific details can be found in the user manual [28]. This means that the data in rural or desert areas is more sparse than that for urban or other areas with high contrast.

B. SMOKE RESULTS IN SUBSTANTIAL REDUCTIONS IN PV CAPACITY

Visual inspection of the satellite imagery retrieved from GOES-17 revealed high concentration of smoke visible for several days during the case study time period. Fig. 4 presents a timeline of the event horizon with a representative sample of the satellite imagery. While the visual imagery provide confirmation, in order to allow this approach to be implemented at scale, aerosol optical density is used as a quantification of the density of aerosols present at a given point in time.

As the aim is to estimate the peak PV capacity for each site, the daily solar production values between 12pm and 1pm were extracted for each assessment period. After accounting for days with incomplete aerosol optical density coverage and other missing or erroneous data, 114 datapoints remain for the two-week period and 508 for the two-month period. In order to validate the statistical assumptions made in the methodology, a Spearman rank-order correlation test is performed to identify the relationship between aerosol optical density and PV output. The results indicate a statistically significant correlation of -0.764, and -0.446, between aerosol optical density and PV for Scenario A and B respectively, indicating that higher levels of smoke aerosols result in a reduction in peak solar PV capacity. It can be seen that the strength of correlation decreases for Scenario B. This is due to the addition of significant periods with limited wildfire smoke as most of the fires effecting the selected PV sites occurred during the period covered by Scenario A. Nonetheless, the relationship remained significant for both periods. Three models are evaluated: 1) Quantile regression (QR); 2) Piecewise linear regression (PLR); and 3) A linear regression model (LR).

1) SCENARIO A: SIGNIFICANT WILDFIRE PERIOD

The results can be seen in Fig. 5 when fit for the entire data. When looking at the overall relationship between aerosol optical density and normalized PV capacity, there is a generally linear relationship which explains why the fit for the models is similar. However, unlike the other models, the PLR reflects an increasing saturation in smoke effects after an aerosol optical density of approximately 1.0. Prior to this value, there is a sharper decline in performance. However, PLR methods are subject to high volatility when fitting the location and slope of each segment as will be demonstrated in Scenario B. Each of the three models handle boundary conditions in a slightly different manner. At an AOD of 0,

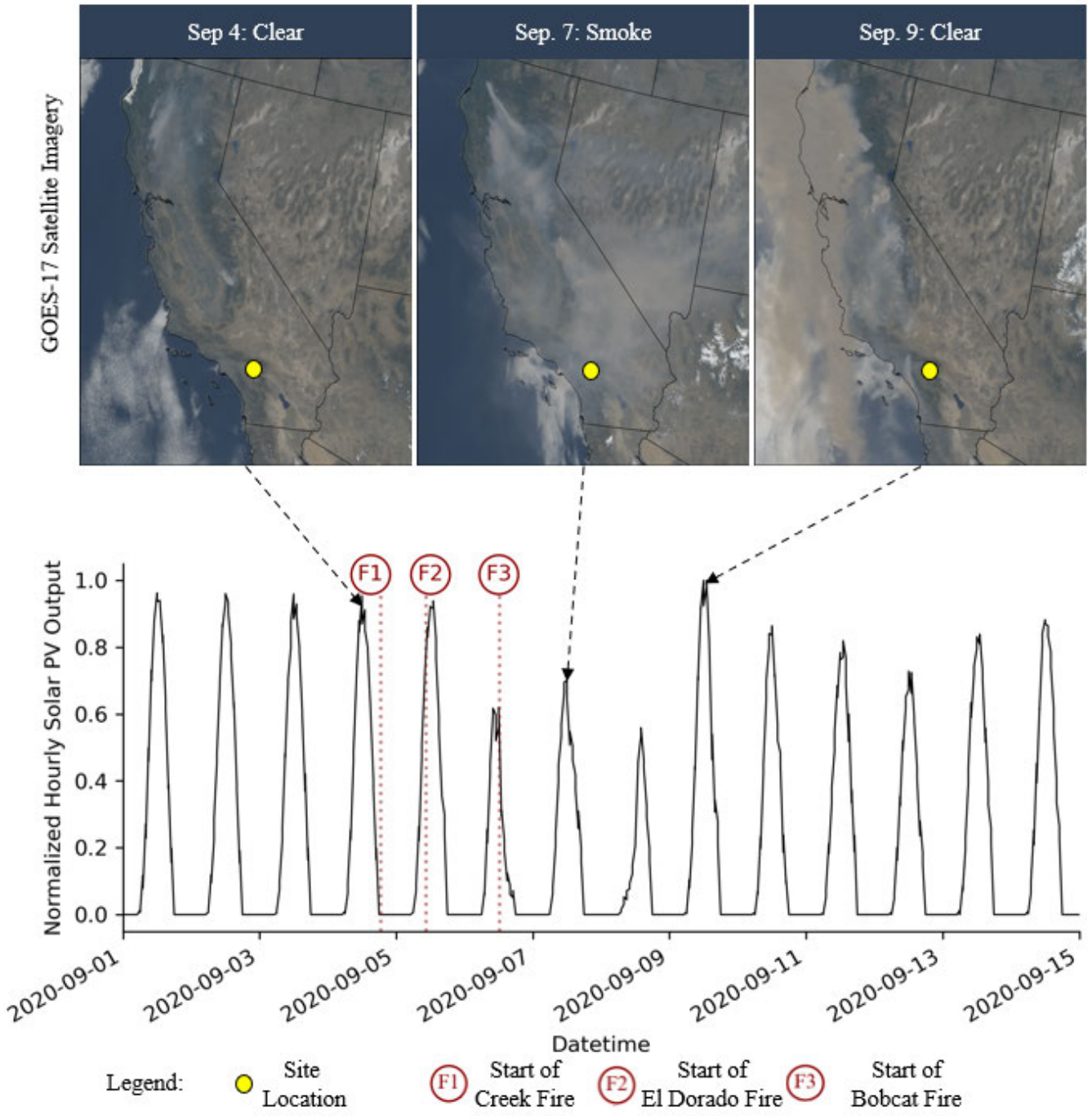

FIGURE 4. Depiction of the impact of wildfire on PV performance for one of the solar PV site regions during scenario A. satellite imagery from NOAA GOES-17 satellite [28] and fire start dates from [48]–[50].

the LR model projects full capacity, whereas the PLR and QR model project a value slightly above 100%. On a perfectly clear day (aerosol optical density of 0), there should not be any derate associated with wildfire smoke.

The error for each model is compared both in sample for the entire data and out of sample using the proposed stratified cross validation with the proposed QR model showing the highest accuracy in both cases. The in sample results for the MAE error for each model as follows: 1) LR: 5.67% 2) QR: 5.37% and 3) PLR: 5.39%. For the out of sample cross-validated results, ten folds were developed, with each fold containing data for nine sites and holding one site out for testing. Each of the models was then fit on the training data and the performance evaluated against the test data for each fold. Although there is some variation across folds, the QR model showed the highest accuracy overall with a

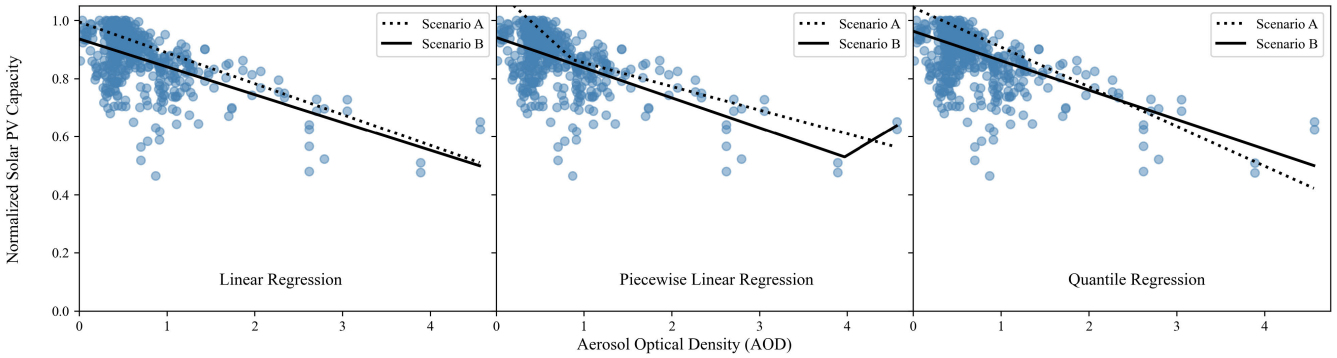

FIGURE 5. Model results.

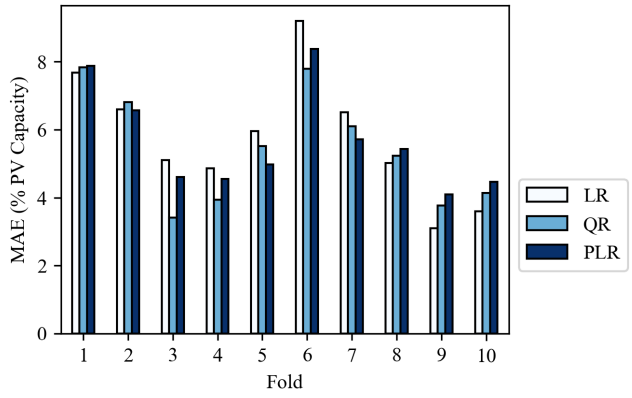

FIGURE 6. Model accuracy over the test data from each fold in the cross-validation for scenario A.

MAE of 5.45% across the folds. The performance for each of the models can be seen in Fig. 6.

2) SCENARIO B: LONGER DURATION EVALUATION

Although the most significant wildfire smoke events were observed during the two week period covered by Scenario A, consideration of a longer duration of operating data provides a more thorough evaluation of the models performance. Furthermore, this longer period serves to demonstrate the significance of normalization when considering capacity and the robustness of each model.

The in sample results for the MAE error for each model as follows: 1) LR: 6.14% 2) QR: 5.85% and 3) PLR: 6.08%. Cross validation was then performed in the same fashion as Scenario A, and the QR model showed the highest accuracy overall with a MAE of 5.88% compared to 6.09% for PLR. This is indicative that the QR model is robust to variations in the test data. Comparison of the overall models for each scenario can be seen in Fig. 5.

The first difference observed in the longer case study was the significant effect on the change in clear sky solar irradiance from August 1st to September 28th. In order to seasonally normalize the PV data as outlined in (2), 15 years of clear sky GHI values were obtained from NREL'S National Solar Radiation Database (NSRDB) over the period of 2005-2019 for each of the PV locations [52]. Data for 2020 was not yet available at the time this study was performed. From the start to the end of the period of time considered in Case Study A there was a mean reduction of 5% in the CGHI whereas for Case Study B a mean reduction of 17% was observed. This demonstrates the significance of seasonal normalization over longer study periods.

The next difference observed in this case study is the robustness of the fit produced by each model. When comparing the model fit from the two case studies, it can be seen that the PLR model is unlikely to provide an optimal fit due to the noise present by additional smoke free days. This can be seen in Fig. 5. Furthermore, it can be seen that the PLR model experienced significant volatility from one set of training data to the next. This indicates that this approach may be prone to overfit the data. By contrast, QR demonstrates high accuracy without sacrificing model robustness, with the fit and corresponding derate remaining stable over both case studies. Hence, we propose that QR can provide operators with an accurate method to use in practice that is more robust to the presence of noise in the training data.

Although we trained this model for two study periods during California's 2020 wildfire season, we believe that the framework is extensible to allow model training for other regions of the world as the underlying foundation of the model's usefulness comes from the ability to translate historical observations of the relationship between aerosols and solar PV performance into a practical quantification of capacity impacts for use by grid operators and planners.

To calculate the corresponding derate factor predicted by each model, the anticipated output at varying aerosol optical densities is subtracted from the maximum power output (100%). These derate factors are shown in Table 1.

C. SOLAR PHOTOVOLTAIC CAPACITY REDUCTION MAPS

The development of a suitable model as described in Section III enables power system planners, operators and other major stakeholders such as generator owners or policy makers to gain insight into the anticipated solar PV capacity derates one might expect for a given time horizon. We present

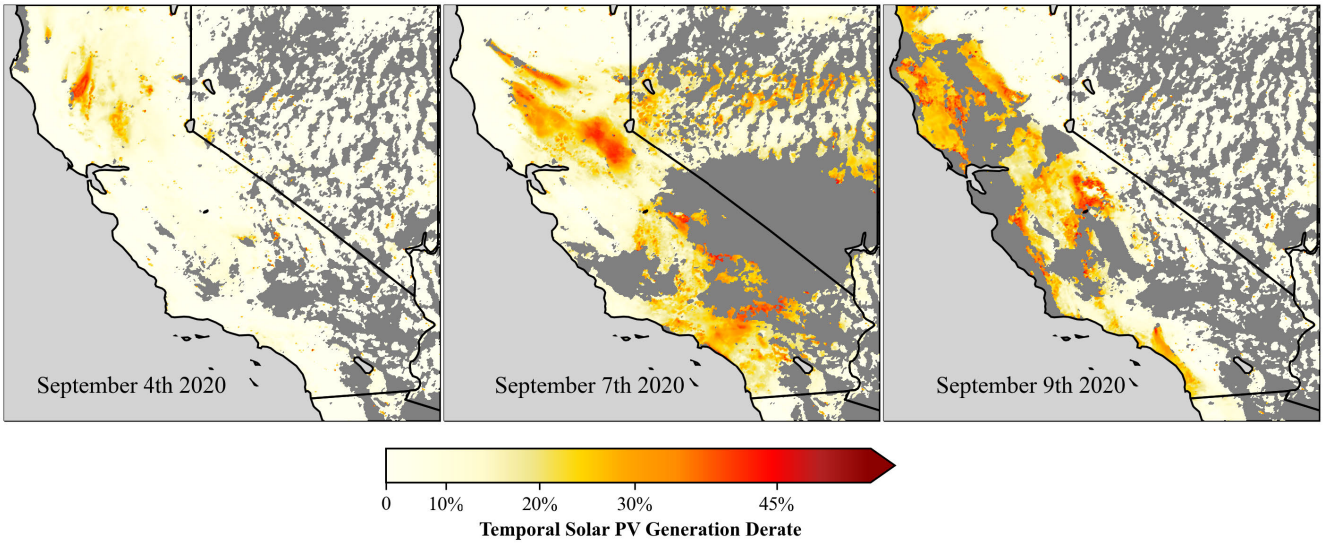

FIGURE 7. Example geospatial smoke derate map for operational use over the period from 12pm to 1pm on three separate days.

TABLE 1. Solar PV derate factors for each model based on scenario B.

	PV Derate Factor		
AOD	Piecewise Linear Regression	Linear Regression	Quantile Regression
0.5	11%	11%	9%
1	16%	16%	14%
2.5	32%	30%	29%
4	46%	45%	44%
4.5	37%	50%	49%

two potential use cases for such information demonstrating the clear benefits such a model can provide.

1) OPERATIONAL GEOSPATIAL SMOKE DERATE MAP

The second contribution of this work is the creation of geospatial smoke derate maps for use in power system operations. The primary use case comes in the operational planning by balancing authorities and utilities which are responsible for generation scheduling to meet their area demand. Sudden unanticipated reductions in solar PV generation capacity due to wildfire smoke can lead to power system security problems if there is not sufficient operating reserve margin. These problems could include generation capacity shortages, unexpected system dispatches, and load shedding. Furthermore, as wildfires can lead to other associated power system impacts such as loss of transmission capability, the loss of additional generation can exacerbate existing problems.

Hence, it is important to accurately anticipate solar generation capacity during the period of the wildfire. Knowing how the associated smoke might affect solar facilities over a large geographic region of the electric grid can aid balancing authorities in making scheduling and dispatch decisions. By feeding the trained model laid out in Section III with aerosol optical density data for a specific point in time across a particular region, the widespread effects of smoke on an entire service territory can be obtained. As the underlying aerosol data is presented at 2 km resolution, this also allows an operator to focus in on a smaller geographic region where a large amount of critical solar PV facilities are located.

2) GEOSPATIAL NOMOGRAM FOR USE IN SOLAR PV SITING

The third contribution of this work is the creation of geospatial nomograms for use in generation siting. The anticipated output of a solar PV generating facility can be a critical input into the economic feasibility studies and siting studies performed by power system planners and generation owners. Current generation siting studies can rely upon historical typical meteorological year calculations such as those present in the NSRDB to account for the anticipated historical performance under ''typical'' weather conditions [52]. Our model can provide additional potentially useful information for high fire risk areas through the creation of a wildfire season geospatial nomogram shown in Fig. 8. This map is created by taking mean daily aerosol optical density from the period of 12pm to 1pm over the period from April 30th to September 28th, 2020. Fig. 8 provides a proof of concept for this map for a single fire season. This can be used to gain an understanding of considerations when siting new solar facilities.

In practice, developers could apply this methodology based on their particular PV siting needs. A developer may want to exclude points which are missing data above a certain number of days over the season. Developers could also apply this methodology for specific periods where a particular type of weather condition is present to gain more insight. The specific choice of duration and fire season used in creation of such a map is linked to the risk tolerance and goals of a particular developer. If a developer wanted to create a conservative estimate of production, a historically bad fire season such as 2020 could be used. To calculate a ''typical'' derate for a wide geographic area, this methodology would be applied over the

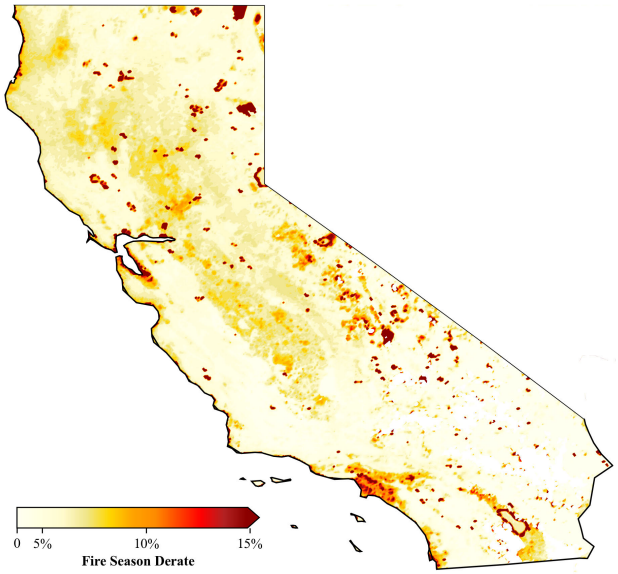

FIGURE 8. Modelled average derate of Solar PV capacity over the period of april 30 - september 28, 2020.

course of 10 historical fire seasons to capture variation in fire season from one year to the next.

IV. MODEL IMPLICATIONS AND REFLECTION

As it is evident that smoke can have a significant impact on the performance of PV production, accurate forecasting of the spread of wildfire smoke will become increasingly important with the continued decarbonization of the electric grid. To this aim, NOAA introduced their smoke forecasting system to provide a daily forecast of the transport and dispersion of smoke from large wildfires [7]. This modelling uses a variety of meteorological variables measured at differing pressure levels but requires at a minimum three-dimensional fields of the vector wind components and temperature [7] as wind plays a key role in the transport of smoke. A history of NOAA's underlying Hybrid Single-Particle Lagrangian Integrated Trajectory model (HYSPLIT) along with applications to the atmospheric transport, dispersion and deposition of pollutants and hazardous materials can be found in [53]. Recently, NOAA has improved its smoke forecasting system to model transport pathways of smoke plumes [54]. As the granularity and accuracy of such products improve, it will enable grid operators to place more confidence in the anticipated solar derate.

We believe that the increasing coverage of satellite and weather station data will serve to address one of the primary limitations in the current work which is incomplete coverage of historical aerosol optical density data. Due to the collection and measurement methods, aerosol optical density data was unavailable for significant portions of the state as observed by the gray areas in Fig. 7. One method of addressing these data gaps might be to use some aerosol optical density approximation or interpolation technique. However, for this work we did not apply this method in order to avoid introducing additional approximation error into the model at this point in time. Further research will evaluate of the trade-offs between geospatial interpolation and model accuracy.

As utilities deploy additional weather stations and satellites continue to improve, enhancement of the underlying data used in the creation of this model will enable more accurate prediction. For example, the Advanced Baseline Imager (ABI) present in the GOES-R Series satellites used in this work, "collects three times more data and provides four times better resolution and more than five times faster coverage than previous GOES" [55]. Hence, we anticipate that the satellite data available in the future will allow for more refinements to the model accuracy.

One other implication from the significant periods of wildfire smoke is the derate of the solar panels due to soiling. This is another reason why wildfires pose a threat to solar PV capacity beyond that of simple clouding. Given the lack of historical data surrounding when cleaning of the panels took place, our model does not assume further degradation of capacity due to soiling. However, when considering the longer term effects of wildfire smoke, soiling would further reduce the capacity of the panels until cleaning is performed as indicated in [56].

V. CONCLUSION

Wildfires pose a significant risk to the resilient operation of the electric grid. Although PV generation facilities may not be sited in high fire risk zones, the smoke from wildfires can travel significant distances and affect large geographic regions. We propose a geospatial wildfire PV capacity model reflecting anticipated temporal derates to solar PV performance due to wildfire smoke. The model's high accuracy is proven using real solar PV operating history and wildfire data. Our work provides power system planners and operators with a more complete understanding of the challenge that wildfire smoke poses as grid operators seek to balance load and generation.

We demonstrate two practical examples of how this model can add value to power system operators and generation developers. The model translates satellite imagery and forecasts of smoke density from wildfires into reductions in PV capacity, potentially enhancing grid operator scheduling decisions and short term forecasts. As meteorological agencies continue to enhance their forecasts of smoke location, the ability to accurately predict PV capacity during extreme wildfires will improve. Finally, the model can provide an estimate of the seasonal capacity reductions for a given location due to smoke, aiding developers in effectively siting new generation facilities. As solar PV generation levels grow in the future, the ability to accurately plan for temporal derates due to wildfire smoke will grow in importance and the proposed framework provides a foundation for future considerations.

ACKNOWLEDGMENT

Southern California Edison for provision of the solar PV operating data; and the NOAA Aerosol and Atmospheric

Composition Science Team for provision of Python code for processing ABI data files as part of the ISS3 Workshop on New Generation Satellite Products for Operational Fire and Smoke Applications conducted on April 20, 2020 (available at https://www.star.nesdis.noaa.gov/smcd/spb/aq/STAR_Python_Hub/index.php).

REFERENCES

[1] "Fires, forests, and the future: A crisis raging out of control?" WWF, BCG, Gland, Switzerland, 2020. Accessed: Feb. 27, 2021. [Online]. Available: https://wwfeu.awsassets.panda.org/downloads/wwf_fires_forests_and_the_future_report.pdf

[2] North American Electric Reliability Corporation, "Transmission system planning performance requirements," NERC, Atlanta, Georgia, Tech. Rep. TPL-001-5, Jan. 2020. [Online]. Available: https://www.nerc.com/pa/Stand/Reliability%20Standards/TPL-001-5.pdf

[3] S. H. Doerr and C. Santín, "Global trends in wildfire and its impacts: Perceptions versus realities in a changing world," *Phil. Trans. Roy. Soc. B, Biol. Sci.*, vol. 371, no. 1696, Jun. 2016, Art. no. 20150345, doi: 10.1098/rstb.2015.0345.

[4] J. T. Abatzoglou, A. P. Williams, and R. Barbero, "Global emergence of anthropogenic climate change in fire weather indices," *Geophys. Res. Lett.*, vol. 46, no. 1, pp. 326–336, Jan. 2019. [Online]. Available: https://onlinelibrary.wiley.com/doi/abs/10.1029/2018GL080959

[5] W. M. Jolly, M. A. Cochrane, P. H. Freeborn, Z. A. Holden, T. J. Brown, G. J. Williamson, and D. M. J. S. Bowman, "Climate-induced variations in global wildfire danger from 1979 to 2013," *Nature Commun.*, vol. 6, no. 1, pp. 1–11, Jul. 2015. [Online]. Available: http://www.nature.com/naturecommunications

[6] CAL FIRE. (2021). *Top 20 Largest California Wildfires*. [Online]. Available: https://www.fire.ca.gov/media/4jandlhh/top20_acres.pdf

[7] G. D. Rolph, R. R. Draxler, A. F. Stein, A. Taylor, M. G. Ruminski, S. Kondragunta, J. Zeng, H.-C. Huang, G. Manikin, J. T. McQueen, and P. M. Davidson, "Description and verification of the NOAA smoke forecasting system: The 2007 fire season," *Weather Forecasting*, vol. 24, no. 2, pp. 361–378, Apr. 2009. [Online]. Available: https://journals.ametsoc.org/view/journals/wefo/24/2/2008waf2222165_1.xml

[8] NOAA/NESDIS. *Office of Satellite and Product Operations—Hazard Mapping System*. Accessed: Feb. 27, 2021. [Online]. Available: https://www.ospo.noaa.gov/Products/land/hms.html#about

[9] IEA, "Solar PV," IEA, Paris, France, 2020. Accessed: Feb. 27, 2021. [Online]. Available: https://www.iea.org/reports/solar-pv

[10] G. G. Kim, J. H. Choi, S. Y. Park, B. G. Bhang, W. J. Nam, H. L. Cha, N. Park, and H.-K. Ahn, "Prediction model for PV performance with correlation analysis of environmental variables," *IEEE J. Photovolt.*, vol. 9, no. 3, pp. 832–841, May 2019.

[11] S. Dubey, J. N. Sarvaiya, and B. Seshadri, "Temperature dependent photovoltaic (PV) efficiency and its effect on PV production in the world—A review," *Energy Procedia*, vol. 33, pp. 311–321, Jan. 2013.

[12] S. Mekhilef, R. Saidur, and M. Kamalisarvestani, "Effect of dust, humidity and air velocity on efficiency of photovoltaic cells," *Renew. Sustain. Energy Rev.*, vol. 16, no. 5, pp. 2920–2925, Jun. 2012. [Online]. Available: https://www.sciencedirect.com/science/article/pii/S1364032112001050

[13] N. Gökmen, W. Hu, P. Hou, Z. Chen, D. Sera, and S. Spataru, "Investigation of wind speed cooling effect on PV panels in windy locations," *Renew. Energy*, vol. 90, pp. 283–290, May 2016. [Online]. Available: https://www.sciencedirect.com/science/article/pii/S0960148116300179

[14] N. Heidari, J. Gwamuri, T. Townsend, and J. M. Pearce, "Impact of snow and ground interference on photovoltaic electric system performance," *IEEE J. Photovolt.*, vol. 5, no. 6, pp. 1680–1685, Nov. 2015.

[15] "Standard test methods for electrical performance of nonconcentrator terrestrial photovoltaic modules and arrays using reference cells," Amer. Soc. Test. Mater., West Conshohocken, PA, USA, Tech. Rep. ASTM-E-1036M-96/XAB TRN: 81731476, 1996.

[16] W. T. Jewell and T. D. Unruh, "Limits on cloud-induced fluctuation in photovoltaic generation," *IEEE Trans. Energy Convers.*, vol. 5, no. 1, pp. 8–14, Mar. 1990.

[17] A. Tuohy, J. Zack, S. E. Haupt, J. Sharp, M. Ahlstrom, S. Dise, E. Grimit, C. Mohrlen, M. Lange, M. G. Casado, J. Black, M. Marquis, and C. Collier, "Solar forecasting: Methods, challenges, and performance," *IEEE Power Energy Mag.*, vol. 13, no. 6, pp. 50–59, Nov. 2015.

[18] H. Wen, Y. Du, X. Chen, E. Lim, H. Wen, L. Jiang, and W. Xiang, "Deep learning based multistep solar forecasting for PV ramp-rate control using sky images," *IEEE Trans. Ind. Informat.*, vol. 17, no. 2, pp. 1397–1406, Feb. 2021.

[19] *Forest Service Research Data Archive*. Accessed: Feb. 27, 2021. [Online]. Available: https://www.fs.usda.gov/rds/archive/catalog/RDS-2013-0009.4

[20] D. Rieger, A. Steiner, V. Bachmann, P. Gasch, J. Förstner, K. Deetz, B. Vogel, and H. Vogel, "Impact of the 4 April 2014 Saharan dust outbreak on the photovoltaic power generation in Germany," *Atmos. Chem. Phys.*, vol. 17, no. 21, pp. 13391–13415, Nov. 2017. [Online]. Available: https://acp.copernicus.org/articles/17/13391/2017/

[21] I. Neher, T. Buchmann, S. Crewell, B. Pospichal, and S. Meilinger, "Impact of atmospheric aerosols on solar power," *Meteorologische Zeitschrift*, vol. 28, no. 4, pp. 305–321, Nov. 2019.

[22] J. X. L. Wang, "Mapping the global dust storm records: Review of dust data sources in supporting modeling/climate study," *Current Pollut. Rep.*, vol. 1, no. 2, pp. 82–94, Jun. 2015. [Online]. Available: https://link.springer.com/article/10.1007/s40726-015-0008-y

[23] X. Li, F. Wagner, W. Peng, J. Yang, and D. L. Mauzerall, "Reduction of solar photovoltaic resources due to air pollution in China," *Proc. Nat. Acad. Sci. USA*, vol. 114, no. 45, pp. 11867–11872, Nov. 2017, doi: 10.1073/pnas.1711462114.

[24] I. M. Peters, S. Karthik, H. Liu, T. Buonassisi, and A. Nobre, "Urban haze and photovoltaics," *Energy Environ. Sci.*, vol. 11, no. 10, pp. 3043–3054, Oct. 2018, doi: 10.1039/C8EE01100A.

[25] M. Perry and A. Troccoli, "Impact of a fire burn on solar irradiance and PV power," *Sol. Energy*, vol. 114, pp. 167–173, Apr. 2015.

[26] S. York. (Sep. 2020). *Smoke From California Wildfires Decreases Solar Generation in CAISO—Today in Energy—U.S. Energy Information Administration (EIA)*. [Online]. Available: https://www.eia.gov/todayinenergy/detail.php?id=45336

[27] Z. Tao, H. He, C. Sun, D. Tong, and X.-Z. Liang, "Impact of fire emissions on U.S. air quality from 1997 to 2016—A modeling study in the satellite era," *Remote Sens.*, vol. 12, no. 6, p. 913, Mar. 2020.

[28] M. Carlomusto, "GOES-R series product definition users' guide," Harris Corp., US DOC, NOAA, NESDIS, NASA, Washington, DC, USA, Tech. Rep. 416-R-PUG-L2 Plus-0349, Revision 2.2, Dec. 2019, vol. 5. [Online]. Available: https://www.goes-r.gov/products/docs/PUG-L2+-vol5.pdf

[29] NOAA Global Monitoring Laboratory. *SURFRAD Aerosol Optical Depth*. Accessed: Feb. 27, 2021. [Online]. Available: https://www.esrl.noaa.gov/gmd/grad/surfrad/aod/

[30] NREL. *Solar Resource Glossary*. Accessed: Feb. 27, 2021. [Online]. Available: https://www.nrel.gov/grid/solar-resource/solar-glossary.html

[31] B. Marion, "Influence of atmospheric variations on photovoltaic performance and modeling their effects for days with clear skies," in *Proc. 38th IEEE Photovoltaic Spec. Conf.*, Jun. 2012, pp. 003402–003407.

[32] H.-D. Mohring, D. Stellbogen, R. Schäffler, S. Oelting, R. Gegenwart, P. Konttinen, T. Carlsson, M. Cendagorta, and W. Herrmann, "Outdoor performance of polycrystalline thin film PV modules in different European climates," in *Proc. 19th Eur. PV Sol. Energy Conf. Exhib.*, Paris, France, Jun. 2004, pp. 2098–2100.

[33] J. A. Kratochvil, W. E. Boyson, and D. L. King, "Photovoltaic array performance model," Sandia Nat. Lab., Albuquerque, NM, USA, Tech. Rep. SAND2004-3535, Aug. 2004. [Online]. Available: https://www.osti.gov/biblio/919131

[34] J. Han, M. Kamber, and J. Pei, *Data Mining: Concepts and Techniques*, 3rd ed. Waltham, MA, USA: Morgan Kaufmann, 2011.

[35] R. Koenker and G. Bassett, "Regression quantiles," *Econometrica, J. Econ. Soc.*, vol. 46, no. 1, pp. 33–50, 1978.

[36] B. Liu, J. Nowotarski, T. Hong, and R. Weron, "Probabilistic load forecasting via quantile regression averaging on sister forecasts," *IEEE Trans. Smart Grid*, vol. 8, no. 2, pp. 730–737, Mar. 2017.

[37] T. Mutavhatsindi, C. Sigauke, and R. Mbuvha, "Forecasting hourly global horizontal solar irradiance in South Africa using machine learning models," *IEEE Access*, vol. 8, pp. 198872–198885, 2020.

[38] C. F. Jekel and G. Venter. (2019). *A Python Library for Fitting 1D Continuous Piecewise Linear Functions*. [Online]. Available: https://github.com/cjekel/piecewise_linear_fit_py

[39] R. J. Hyndman and G. Athanasopoulos, *Forecasting: Principles and Practice*. Melbourne, VIC, Australia: OTexts, 2018.

[40] S. van der Walt, S. C. Colbert, and G. Varoquaux, "The NumPy array: A structure for efficient numerical computation," *Comput. Sci. Eng.*, vol. 13, no. 2, pp. 22–30, Mar. 2011.

[41] W. McKinney, "Data structures for statistical computing in Python," in *Proc. 9th Python Sci. Conf.* 2010, pp. 50–59.
[42] K. Jordahl *et al.*, "Geopandas/geopandas: v0.6.1," Zenodo, Oct. 2019, doi: 10.5281/zenodo.3483425.
[43] Met Office. (2015). *Cartopy 0.15.0*. [Online]. Available: http://scitools.org.uk/cartopy
[44] J. D. Hunter, "Matplotlib: A 2D graphics environment," *Comput. Sci. Eng.*, vol. 9, no. 3, pp. 90–95, 2007.
[45] S. Seabold and J. Perktold, "Statsmodels: Econometric and statistical modeling with Python," in *Proc. 9th Python Sci. Conf.*, 2010, pp. 92–96. [Online]. Available: https://www.statsmodels.org/stable/index.html#citation
[46] P. Virtanen, R. Gommers, T. E. Oliphant, M. Haberland, T. Reddy, D. Cournapeau, E. Burovski, P. Peterson, W. Weckesser, J. Bright, and S. J. van der Walt, "SciPy 1.0: Fundamental algorithms for scientific computing in Python," *Nature Methods*, vol. 17, no. 3, pp. 261–272, Mar. 2020, doi: 10.1038/s41592-019-0686-2.
[47] National Interagency Fire Center. (2021). *2020 Perimeters to Date—Public NIFS Archive Perimeters*. Accessed: Jan. 2021. [Online]. Available: https://data-nifc.opendata.arcgis.com/
[48] National Wildfire Coordinating Group. (2020). *Creek Fire Information—InciWeb the Incident Information System*. Accessed: Jan. 2021. [Online]. Available: https://inciweb.nwcg.gov/incident/7147/
[49] National Wildfire Coordinating Group. (2021). *El Dorado Fire Information—InciWeb the Incident Information System*. Accessed: Jan. 2021. [Online]. Available: https://inciweb.nwcg.gov/incident/7148/
[50] National Wildfire Coordinating Group. (2020). *Bobcat Information—InciWeb the Incident Information System*. Accessed: Jan. 2021. [Online]. Available: https://inciweb.nwcg.gov/incident/7152/
[51] Global Modeling and Assimilation Office, "MERRA-2 tavg1_2D_slv_Nx: 2D, 1-hourly, time-averaged, single-level, assimilation, single-level diagnostics V5.12.4," Goddard Earth Sci. Data Inf. Services Center, Greenbelt, MD, USA, Dec. 2015. Accessed: Apr. 20, 2021, doi: 10.5067/VJAFPLI1CSIV.
[52] M. Sengupta, Y. Xie, A. Lopez, A. Habte, G. Maclaurin, and J. Shelby, "The national solar radiation data base (NSRDB)," *Renew. Sustain. Energy Rev.*, vol. 89, pp. 51–60, Jun. 2018, doi: 10.1016/j.rser.2018.03.003.
[53] A. F. Stein, R. R. Draxler, G. D. Rolph, B. J. Stunder, M. D. Cohen, and F. Ngan, "NOAA's HYSPLIT atmospheric transport and dispersion modeling system," *Bull. Amer. Meteorol. Soc.*, vol. 96, no. 12, pp. 2059–2077, Apr. 2015.
[54] H. C. Kim, T. Chai, A. Stein, and S. Kondragunta, "Inverse modeling of fire emissions constrained by smoke plume transport using HYSPLIT dispersion model and geostationary satellite observations," *Atmos. Chem. Phys.*, vol. 20, no. 17, pp. 10259–10277, Sep. 2020.
[55] NOAA & NASA. *FAQs | GOES-R Series*. Accessed: Feb. 27, 2021. [Online]. Available: https://www.goes-r.gov/resources/faqs.html
[56] M. R. Maghami, H. Hizam, C. Gomes, M. A. Radzi, M. I. Rezadad, and S. Hajighorbani, "Power loss due to soiling on solar panel: A review," *Renew. Sustain. Energy Rev.*, vol. 59, pp. 1307–1316, Jun. 2016.

DANIEL L. DONALDSON (Graduate Student Member, IEEE) received the B.S. degree in electrical and computer engineering, in 2012, and the master's degree in electrical engineering, in 2015. He is currently pursuing the Ph.D. degree with the University of Birmingham, Birmingham, U.K., with a focus on resilience of electric power systems. He worked at Southern California Edison (SCE) for seven years in a variety of roles, including work in distribution engineering, transmission planning, and demand and DER forecasting. He is a licensed Professional Engineer in the State of California.

DAVID M. PIPER received the B.S. degree in electrical engineering from California Polytechnic Pomona and the master's degree in electrical engineering from the University of Idaho. He has been with Southern California Edison (SCE), since 2009. He is currently a Senior Operating Engineer with the SCE's Grid Control Center. He is also a licensed Professional Engineer in the State of California.

DILAN JAYAWEERA (Senior Member, IEEE) received the Ph.D degree from the University of Manchester Institute of Science and Technology (UMIST), U.K., in 2003. He is currently a Senior Lecturer in electrical power systems with the Department of Electronic, Electrical and Systems Engineering (EESE), University of Birmingham. He has wide experiences in energy industry, research, and teaching. He has authored a significant number of research articles in scientific journals, conference proceedings, and book chapters in the fields of power system security, reliability, active distribution network operation, smart grids, smart asset management, and risks in power systems. He is a Chartered Engineer in U.K., a Chartered Professional Engineer in Australia, and a Fellow at Engineers, Australia. He is an Editor of the IEEE TRANSACTIONS ON POWER SYSTEMS and *Power Engineering Letters*.